LYMAN ALPHA EMISSION FROM ULIRGS AT Z =0.15

A THESIS
SUBMITTED TO THE FACULTY OF THE GRADUATE SCHOOL
OF THE UNIVERSITY OF MINNESOTA
BY

Sourabh Singh Chauhan

IN PARTIAL FULFILLMENT OF THE REQUIREMENTS
FOR THE DEGREE OF
Master Of Science

Dr. Claudia Scarlata

February, 2020

Acknowledgements

This research has made use of the NASA/IPAC Extragalactic Database (NED), which is operated by the Jet Propulsion Laboratory (JPL), California Institute of Technology, under contract with the National Aeronautics and Space Administration (NASA). This work was supported by the NASA and MIfA, University of Minnesota. SC is thankful to all the resources provided by MiFA to make this research possible. SC is especially thankful to continuous discussions with advisor Prof. Claudia Scarlata. SC is thankful to M. Hayes for providing us with data for LARS galaxies. And, SC is grateful to the discussions with other grads.

Abstract

Most of high redshift star formation occurs in IR-bright galaxies. Cosmic average star formation peaks around redshift of 2. One of the main tracer of these galaxies is the Lyman-alpha line. Ly-alpha photons are highly susceptible to dust absorption. However, surprising results of recent studies have found that a large fraction of IR- bright galaxies also have Lyα in emission. In the present work we attempt to understand the origin of this Lyα emission using high resolution imaging results from Hubble Space Telescope. Interpretation of Lyα observations is extremely complex as these photons traverse through a large portion of ISM before being able to escape. Resolved imaging in Lyα can help us trace the path of Lyα photons through ISM and conclude the constituents of ISM. This has motivated studies of nearby analog of high redshift galaxies. Only HST provides the UV access and resolution to do this. Several studies of UV-selected galaxies have been carried using HST. UV-selected galaxies are only a small fraction of galaxies at high-z. So far, no study has ever imaged the IR-bright systems in Lyα . We image 5 local ultra luminous infrared galaxies (ULIRGs) on a spatial scales of just 140 pc in Lyα . Preliminary results show that 3 out of 5 ULIRGs in our sample have Lyα in emission globally.

Contents

List of Tables

List of Figures

Chapter 1

Introduction

Studies of star formation history of the Universe have shown that the cosmic average of star formation rate peaks around redshift of 2(Madau & Dickinson (2014)). Observations of galaxies at $z \approx 2$ reveal that the main site for star formation are infrared galaxies (Chary et al. (2007); Berta et al. (2011); Murphy et al. (2011); Magnelli et al. (2011)). Infrared emission from galaxies is produced when UV photons from young stars are absorbed by dust grains and re-emitted in infrared wavelengths. Based on total infrared luminosities, infrared galaxies have two main sub classes - luminous infrared galaxies (LIRGs) with $L_{IR} > 10^{11} L_{\odot}$ and ultra luminous infrared galaxies (ULIRGs) with $L_{IR} > 10^{12} L_{\odot}$[1] . ULIRGs are rare galaxies at present epoch but they dominate cosmic star-formation at higher-z and by $z \approx 2$ the most of the stars are formed in ultra-luminous infrared galaxies Chary et al. (2007).

There are several direct and indirect methods to probe star formation in infrared galaxies. One of the most frequently used method is to identify local analogs of high-z star-forming galaxies (Desai et al. (2007); Pope et al. (2008); Menéndez-Delmestre et al. (2009); Stacey et al. (2010); Díaz-Santos et al. (2010)) and use them as laboratories to study the star formation in the high redshift Universe. Stars are formed in local gravitation potential wells of interstellar medium when the local gravitational energy is able to overcome the potential barrier to start nuclear reactions. Therefore, in order to understand the star formation and galaxy evolution over cosmic time, an extensive study of interstellar medium of galaxies is critical. Multiwavelength imaging and spectroscopy

[1] L_{IR} is defined as total infrared luminosity in wavelength range of 8 μm to 1000

is used to study the ISM in galaxies. Local galaxies provide a well resolved imaging in various wavelength bands. Various infrared telescopes (IRAS, Akari, WISE, Spitzer, Herschel)[2] have observed LIRGs and ULIRGs in local and in high redshift Universe.

The Figure 1.1 shows spectral energy distribution (SED) of a typical infrared galaxy. A small fraction of total bolometric luminosity comes from UV and optical for dusty infrared galaxies. In case of ULIRGs, more than 90 % of the bolometric luminosity comes from infrared emission. Most of the infrared emission in a galaxy is produced when dust particles are heated by UV photons and re-emitted in infrared wavelengths. Therefore, a hard ionizing source is required to produce bulk infrared emission. There can be two types of sources which produce this high energy radiation, 1) nuclear fusion occurring in rapidly formed stars (starbursts), 2) Energy generated by mass accretion on spatially compact, super-massive black holes (SMBHs) (AGN activity). High resolution imaging of such high infrared sources can help us disentangle these two energy sources.

Several studies have used local starburst galaxies [3] as analogs of high redshift galaxies. Recently, a sample of 14 starburst galaxies is studied using Lyα imaging(Hayes et al., 2014). Lyα emission line of atomic hydrogen is produced by decay of photons from n = 2 state to n = 1 state. Star-forming galaxies consist of young massive O, B stars which have short lifetime. These stars produce a large number of ionizing photons which ionize the neutral hydrogen atoms in the interstellar medium (ISM, hereafter). Ionized hydrogen recombines with an electron to produce neutral hydrogen atom. The transition probabilities for radiative cascade from higher energy levels to ground state imply that about 68% [4] of the recombination events[5] produce Lyα photons (Pengelly 1964; Hummer & Storey 1987; Dijkstra 2014). Therefore, more than half of ionizing photons will contribute to a Lyα emission line in the galaxy.

With a large abundance of ionizing photons and hydrogen atoms in the star-forming galaxies, one would expect a star-forming galaxy to be Lyman alpha emitting galaxy as well. However, the optical depth of Lyα photons is too large in typical ISM conditions[6]

[2] wavelength range IRAS- (5-100 μm), Akari - (2- 200 μm), Herschel- (55-672 μm), WISE - (3-25 μm)

[3] Galaxies with very high star formation rates in comparison to average star formation rate of other galaxies.

[4] Assuming case B recombination.

[5] If the recombination event produces neutral hydrogen atom in 2P state, the only way to de-excite the atom is by emission of Lyα photons. This is why this transition is called a resonant transition.

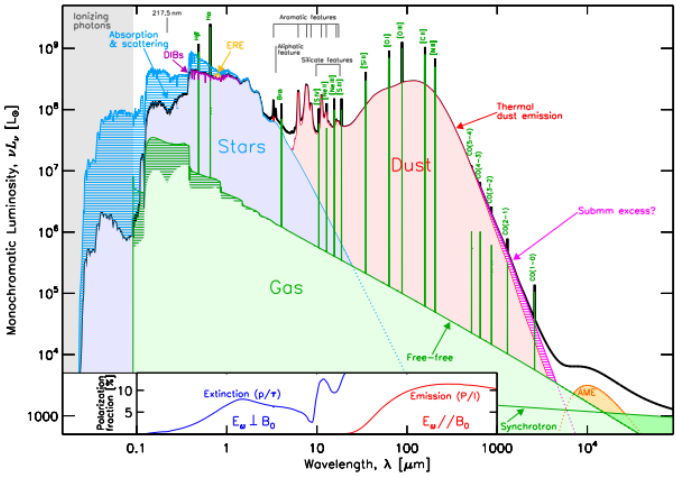

Figure 1.1: The figure shows total Spectral energy distribution (SED, hereafter)of typical dusty galaxy (shown in black) along with the contribution to SED from various stars, gas and dust (shown in blue, green and red respectively). Stars in the galaxy emit as thermal black body radiation. The cumulative contribution of stellar population gives the total stellar contribution to the SED. Dust absorbs and scatters the UV photons of stellar radiation more efficiently than IR photons. This populates the IR part of the SED of galaxy. Interstellar gas contributes to long wavelength continuum by free-free emission and synchrotron emission. It also contributes as molecular emission lines and nebular emission lines. This figure is taken from Figure 1 of Galliano et al. (2017).

. Even when neutral gas at moderate temperature of $T = 10^4 K$ is optically thin to Lyman continuum ($N_{HI} < 1/\sigma_0 \approx 1.59 * 10^{17} cm^{-2}$), the optical depth of Lyα photons is really high

$$\tau_{Ly\alpha} = 9.33 * 10^3 \left(\frac{12.85 km/s}{b}\right) \left(\frac{N_{HI}}{1.59 * 10^{17} cm^{-2}}\right)$$

Where N_{HI} is column density of neutral Hydrogen and b represents thermal velocity at given temperature and density of gas(following Martin et al. 2015). Because of high optical depth Lyα photons undergo several scattering events before they escape the ISM if they are not absorbed by the dust grains. Many scattering events make Lyα emission from galaxies to be sensitive to dust properties of the ISM (Scarlata et al. (2009)), kinematics of neutral hydrogen gas (Verhamme et al. (2006)), clumpiness of ISM (Henry et al. (2015),Natta & Panagia (1984)). Resonant nature of this transition makes the radiative transfer problem extremely complicated.

Based on the fact that high redshift IR bright galaxies have a large amount of dust and that the Lyα photons are absorbed by dust grains, first order inference would be that high redshift star-forming galaxies do not have much Lyα in emission. One also expects larger fraction galaxies with Lyα emission from a sub sample of UV-selected Lyman break galaxies (LBGs). Surprisingly, detection rate for Lyα emission from LBGs is quite low and sensitive to redshift of the galaxy (Stark et al., 2010). By z=3, only 25% of LBGs show Lyα emission (Shapley et al., 2003). Furthermore, Lyα detection rate at $1.8 < z < 5$ for mid-IR and submm-selected galaxies is around 80 %(Chapman et al., 2005; Bridge et al., 2012). All of these observations motivate the Lyα imaging study of spatially resolved emission regions in IR bright galaxy. In particular, ULIRGs provide us with extreme cases of such infrared bright galaxies. However, with the current technology it is not possible to do well resolved imaging study of Lyα emission in high redshift because of the smaller spatial resolution. Therefore, we look for local ULIRG analogs of high-z galaxies to carry out imaging studies.

In spite of ULIRGs being driver of high redshift star formation, there have been no high resolution Lyα imaging of ULIRGs. Martin et al. 2015 studied the spectral properties of ULIRGs in Lyα using the HST COS (Cosmic Origin Spectrograph) observations. They found that infrared emission is produced by clumps of gas condensing out of a

[6] $T = 10^4 K$ $n = 10^4 cm^{-3}$

fast wind and Lyα photons are able to escape through low hydrogen column density cavities in ISM. However, no imaging studies were done. In the present work, we carry out high resolution imaging studies of ULIRGs at low redshifts (i.e. $z \approx 0.15$) and try to understand Lyα radiative transfer through dusty medium.

This thesis proceeds as follows :- in Chapter 2 we describe our survey strategy to obtain HST imaging, in Chapter 3 we discuss our sample of galaxies and method of selecting 5 ULIRGs for HST imaging, Chapter 4 briefly describes HST observations, Chapter 5 describes the data reduction steps to obtain Lyα, α and UV maps, Section 6 describes several local and global measurements on the maps and compare it to various galaxy properties, Chapter 7 the physical understanding on ULIRGs based on measurements on line and continuum maps, in Chapter 9 we conclude the paper with direction of future works and limitations of our methods. Throughput this paper, we adopt a flat ΛCDM cosmology with $\Omega_M = 0.3, \Omega_\lambda = 0.7$ and $H_0 = 70 kms^{-1} Mpc^{-1}$.

Chapter 2

Survey Strategy

We obtain Lyα images of galaxies using the Hubble Space Telescope (HST, hereafter) data. It is difficult to do Lyα and UV imaging using Earth based telescopes because Earth's atmosphere absorbs UV photons very efficiently. The fraction of UV light that passes through atmosphere is dependent on atmospheric conditions and cloud cover. On the other hand, space based telescopes observations are only diffraction limited and have no atmospheric effect. This is why we use HST to obtain Lyα images of ULIRGs.

Our sample selection and survey strategy is restricted based on experience from previous Lyα imaging observations using HST. Östlin et al. 2009; Hayes et al. 2014; Hayes et al. 2009 were one of the first to use HST to obtain Lyα imaging. Östlin et al. 2009 used Solar Blind Channel (SBC, hereafter) of Advance Camera Surveys (ACS, hereafter) to obtain Lyα images of 6 starburst galaxies in the nearby Universe. They used two filters a medium pass filter F122M, a long pass filter F140LP to obtain Lyα line and continuum images respectively. Line flux on each pixel is obtained by :-

$$\texttt{Ly}\alpha = \texttt{online} - \texttt{CTN} \times \texttt{offline} \tag{2.1}$$

where CTN (Continuum Throughput Normalization) (Hayes et al., 2005) is a factor dependent on the age and reddening of the stellar population. Other than low filter response, Lyα images from SBC filters are affected by the following main factors :-

1. Stellar Lyα absorption

2. Long wavelength leaks in filters

3. Contamination from Geocoronal Lyα line and Milky Way Lyα absorption

4. Model dependence of stellar continuum fitting

Stellar Lyα absorption can not be corrected using just imaging methods. Stellar Lyα absorption arises when cold dust clouds hinder stellar emission. These absorption features are stronger for older stellar population because there are more clouds in their environment. A strong Lyα absorption can cancel some or all of the Lyα emission. Spatially resolved spectrum of starburst regions can be used to identify such regions and obtain absorption strength. However, it is not possible to isolate this effect in imaging as we only see combined effect of emission and absorption in an image. Other three effects can be resolved as described below.

The problem of long wavelength leaks and contamination from local Lyα emission and absorption can be solved simultaneously. All of the SBC filters have long wavelength tails as shown in Figure 2.1. This leads to additional flux in filters from longer wavelengths. Rest frame Lyα ($\lambda \approx 1215.67$Å) line passes through the peak of F122M throughput profile (shown in pink in Figure 2.1). Therefore, Lyα image in F122M is highly contaminated by Geocoronal Lyα and Milky way Lyα absorption. The resolution of both of these issues is based on observation the observation that long wavelength tail is identical for all long pass filters in SBC (F125LP, F140LP, F150LP , F165LP) (Hayes et al., 2009). Subtracted images from any two filters will not have long wavelength leaks. Hayes et al. 2009 used long pass filter F125LP and F140LP to obtain line and continuum image respectively. This method not only gets rid of Geocoronal Lyα contamination and Milky way Lyα absorption, but it also solves the issue of long wavelength leaks in filters.

Östlin et al. 2014 improved the method furthermore by introducing synthetic narrow band filters. They created two synthetic narrow band filters ($\mathtt{F}^{\mathtt{L}}_{\mathtt{syn}} = (\mathtt{F125} - \mathtt{F140})$) and ($\mathtt{F}^{\mathtt{R}}_{\mathtt{syn}} = (\mathtt{F140} - \mathtt{F150})$) by subtracting adjacent SBC long pass filter $\mathtt{F125}, \mathtt{F140}, \mathtt{F150}$. For lower (higher) redshift galaxy, $\mathtt{F}^{\mathtt{L}}_{\mathtt{syn}}(\mathtt{F}^{\mathtt{R}}_{\mathtt{syn}})$ gives line (continuum) flux and $\mathtt{F}^{\mathtt{R}}_{\mathtt{syn}}(\mathtt{F}^{\mathtt{L}}_{\mathtt{syn}})$gives line (continuum) flux. This additional continuum flux is used to model stellar continuum and obtain CTN (equation 2.1) more accurately. This method gives a S/N improvement of 7 over F122M Lyα imaging (see appendix of Östlin et al. 2014). However, Continuum subtraction still remains sensitive to shape of spectrum around Lyα wavelength.

To accurately subtract the continuum, stellar populations and dust properties should be known precisely.

In the present work, we improve on synthetic narrow band filter method by introducing a non-parametric method. We use all 4 long pass filters of SBC to obtain 3 synthetic narrow bands ($\mathtt{F}^{\mathtt{L}}_{\mathtt{syn}} = \mathtt{F125} - \mathtt{F140}$, $\mathtt{F}^{\mathtt{line}}_{\mathtt{syn}} = \mathtt{F140} - \mathtt{F150}$, $\mathtt{F}^{\mathtt{R}}_{\mathtt{syn}} = \mathtt{F150} - \mathtt{F165}$). Redshifts of galaxies are chosen such that redshifted Lyα lies in the central synthetic filter. Images in adjacent narrow bands are subtracted pixel by pixel to obtain galaxy images on both sides of Lyα continuum (details in Section **??**). Modelling of stellar continuum is not required in this method because Lyα continuum is obtained by a linear fit between red side and blue side of the continuum. Östlin et al. 2014 used 3 SBC filters so they are able to get continuum only on one side of Lyα [1] and other side is modeled using stellar population models. In this method no stellar population synthesis modelling is required. This non-parametric resolves all the all 3 resolvable issues with Lyα imaging of nearby galaxies.

[1] For higher (lower) redshift galaxies one gets continuum image on the blue (red) side of the Lyα (See Figure 1 in Östlin et al. 2014.

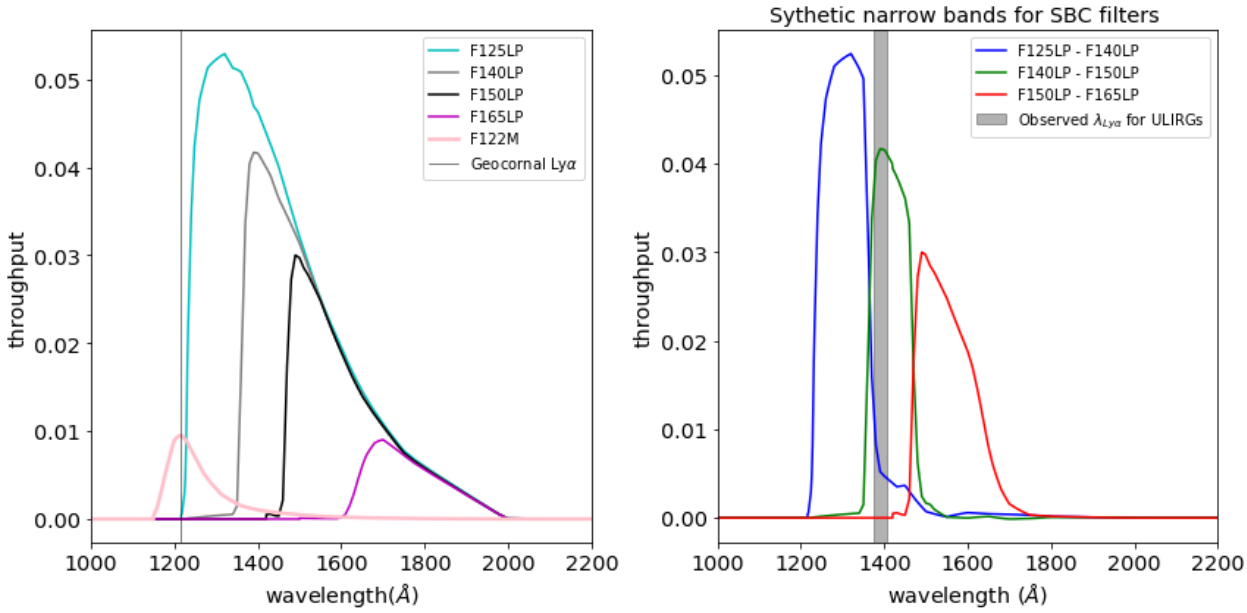

Figure 2.1: The figure shows synthetic narrow band throughputs which are created using low-pass SBC filters. Left side of the figure has throughput profiles for all SBC filters. Östlin et al. 2014 use F125, F140, F150 images along with stellar population models to obtain Lyα continuum. Lyα image in filter F122M is used to compare S/N of new imaging method in Östlin et al. 2014. Right side of the figure shows subtracted synthetic filter throughputs. Vertical Grey shaded area indicates the redshifted Lyα wavelength range for galaxies in our sample.

Chapter 3

Sample Selection

The galaxies studied in this work were selected from the 118 ULIRGs in the IRAS 1 Jy catalog (Kim, Veilleux, & Sanders, 1998). In the IRAS catalog the total IR luminosity is computed from a linear combination of the flux densities at 12, 25, 60 and 100μm[1] . In order to select galaxies for which Lyα imaging can be accomplished using the filter sets available on the Solar Blind Camera (SBC) on HST, we apply three additional selection criteria:

- **Redshift window:** As we explain in Section **??**, our method for isolating Lyα radiation requires galaxies at redshifts that shift the Lyα into the range 1370Å$<$ $\lambda <$ 1460Å, where the narrow band transmission curve is at approximately 90%. This wavelength range corresponds to the redshift interval $0.127 < z < 0.201$.

- **UV efficient:** In order to optimize the efficiency of the UV observations, we selected galaxies for which the Milky Way transmits more than 80% at Lyα. This is achieved by limiting to galaxies in regions of the sky where the galactic color excess $[E(B-V)^{MW}]$ is smaller than 0.025.

- **Star forming:** We next restrict our sample to non- AGN dominated galaxies with based on emission line properties (Veilleux et al., 2002). We use the BPT diagram (named after Baldwin, Phillips & Telervich Baldwin et al. 1981) to identify the main ionization mechanism of the nebular gas. In its most used form, it

[1] $F_{\rm IR} = 1.8 \times (13.48 \times f_{12} + 5.16 \times f_{25} + 2.58 \times f_{60} + f_{100})$

uses ratios of optical emission lines close in wavelength (to minimize the effect of dust extinction) to distinguish between AGNs and star forming galaxies.

We use the [Hα]/[NII] and [OIII]/[Hβ] line ratios, and the separation criterion presented in Kewley et al. 2001, 2006; Kauffmann et al. 2003. Line fluxes were obtained from SDSS spectrum of galaxies in northern hemisphere and 2dFGRS (2 degree field galaxy redshift survey) spectrum for galaxy in Southern hemisphere (ULIRG-5). The position in BPT diagram of the selected targets is shown in Figure 3.1. All the galaxies lie below Kewley+01 line [2] (shown in blue) which indicates their non-AGN dominant nature. We also show Kauffman+03 line [3] (shown in red) which separates AGN composite galaxies with star-forming galaxies. AGN composite galaxies have up to 40 % of their Hα luminosity contribution from an AGN. All SDSS galaxies in BPT diagram are also shown for reference [4] .

Galaxy id	RA	Dec	m_V	m_{AB}^{FUV}	L_{IR} [in L$\odot$]	redshift	ULIRG id
IRASF10594+3818	11 02 14.0550	+38 02 35.21	17.5	19.80	$10^{12.24}$	0.158	1
IRASF12447+3721	12 47 7.7460	+37 05 36.65	18.0	20.36	$10^{12.06}$	0.158	2
IRASF13469+5833	13 48 40.1150	+58 18 52.26	18.0	21.18	$10^{12.15}$	0.157	3
IRASF14202+2615	14 22 31.3620	+26 02 4.98	17.4	19.30	$10^{12.39}$	0.159	4
IRASF22206-2715	22 23 28.9090	-27 00 3.44	18.2	19.47	$10^{12.19}$	0.131	5

Table 3.1: Properties of ULIRGs in the present sample. Apparent magnitude in visible (m_V) was obtained from GALEX. GALEX FUV filter is used to obtain FUV magnitude. Spectroscopic redshifts were obtained using the best fit emission line fitting of SDSS (4 northern hemisphere ULIRGs) and 2dFGRS (2 degree field galaxy redshift survey, for Southern hemisphere ULIRG) spectrum. The last column has the ULIRG id which will be used in further discussions of this paper.

Five galaxies are left after the above selection criteria, with $L_{IR} = 10^{12.05} - 10^{12.4} L_{\odot}$. Basic properties of this sample are listed in Table 3.1. UV properties of galaxies obtained from GALEX survey [5] are listed in Table 3.2. UV slope β listed in table was obtained

[2] $\log([OIII]/[H\beta]) = 0.61/(\log([NII]/[H\alpha]) - 0.47) + 1.19$
[3] $\log([OIII]/[H\beta]) = 0.61/(\log([NII]/[H\alpha]) - 0.05) + 1.3$
[4] SDSS data was downloaded from http://www.sdss.org/dr14/spectro/galaxy_mpajhu/
[5] http://galex.stsci.edu/GR6/?page=mastform

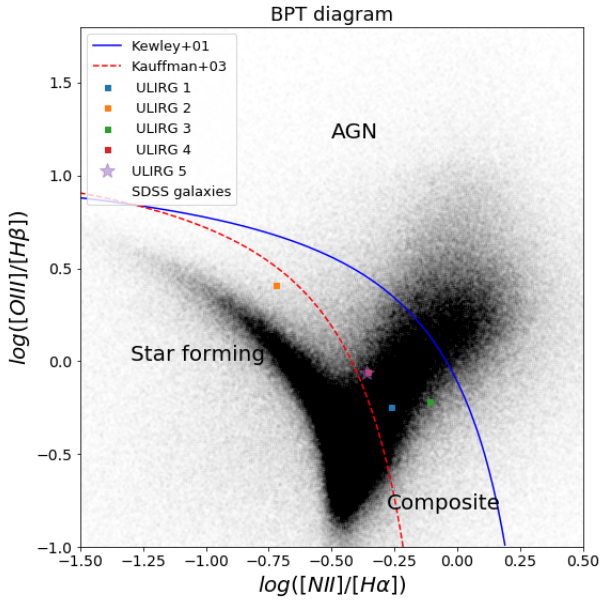

Figure 3.1: The figure shows BPT diagram for ULIRGs. Black dots represent all SDSS galaxies while colored points represent galaxies in our sample. line fluxes were obtained from SDSS spectrum (Norther hemisphere ULIRGs) and 2dFGRS (Southern hemisphere ULIRG). The ULIRG in southern hemisphere is marked with a star. Most of the galaxies lie in the regime of high star formation rate.

Galaxy id	m_{FUV}	m_{NUV}	$E(B-V)^{MW}$	β
IRASF10594+3818	19.80	19.45	0.0144	-1.21
IRASF12447+3721	20.36	19.74	0.0168	-0.60
IRASF13469+5833	21.18	20.48	0.0096	-0.42
IRASF14202+2615	19.30	18.78	0.0156	-0.81
IRASF22206-2715	19.47	19.03	0.0185	0.96

Table 3.2: The table lists apparent UV properties of galaxies obtained from GALEX survey. AB magnitudes in FUV ad NUV bands were used to obtain UV slope β. Milky way extinction ($E(B-V)^{MW}$)is used to avoid milky way dust for galaxy observations.

by fitting UV fluxes in FUV and NUV bands to $f_\lambda \propto \lambda^\beta$ using the pivot wavelengths (definition is given in footnote 1) of FUV and NUV bands defined as $\lambda_p^{NUV} = 1524.0$Å and $\lambda_p^{NUV} = 2297.0$Å. Milky way extinction $E(B-V)^{MW}$ was obtained using infrared maps.

We compare the properties of these galaxies with LIRGs observation data available from archive. Total bolometric luminosity of star-forming galaxies can be well approximated by summing up UV and IR luminosities ($L_{\rm bol} = L_{IR} + L_{FUV}$). Dust in galaxies processes the UV light to produce the infrared emission. Therefore, amount of dust obscuration in galaxies can be roughly represented by ratio of infrared luminosity and UV luminosities ($L_{\rm IR}/L_{\rm FUV}$). Reddy et al. 2006 used very deep *Spitzer* MIPS[6] 24 μm observations to study infrared galaxies at $z \approx 2$. They obtained a linear fit between total bolometric luminosity and ratio of infrared and UV luminosities:-

$$\log L_{\rm bol} = (0.62 \pm 0.06) \log \left(\frac{L_{IR}}{L_{FUV}} \right) + (10.95 \pm 0.07) \tag{3.1}$$

In Figure 3.2, the relation is shown with a black line. We compare dust obscuration properties of ULIRGs in present sample with higher redshift IR bright galaxies (Daddi et al. 2007 $\rightarrow$ $1.4 < z < 2.5$) observed by *Spitzer* and Lyα emitters in the nearby Universe observed by HST.[7] (Östlin et al. 2014, Hayes et.al. 2018 (in prep.) $\rightarrow$ $0.028 < z < 0.181$) IR luminosities for LARS, eLARS and ULIRGs were obtained from

[6] MIPS = Multiband Imaging Photometer for SST (Spitzer Space Telescope)

[7] This sample of 14 Lyα emitters (LAEs, hereafter) is often used as a reference to study LAEs in nearby Universe, thus the name, Lyα reference sample (LARS). eLARS stands for extended LARS which is a survey of 49 HST orbits to study 28 more galaxies. LARS and eLARS combine to form a sample of LAE candidates in nearby Universe.

WISE [8] and IRAS catalogs. FUV luminosities were obtained from GALEX catalog. Galaxies in the current sample are 0.25 to 0.6 dex brighter in infrared than the the most infrared luminous galaxy in LARS and eLARS as shown in Figure 3.2.

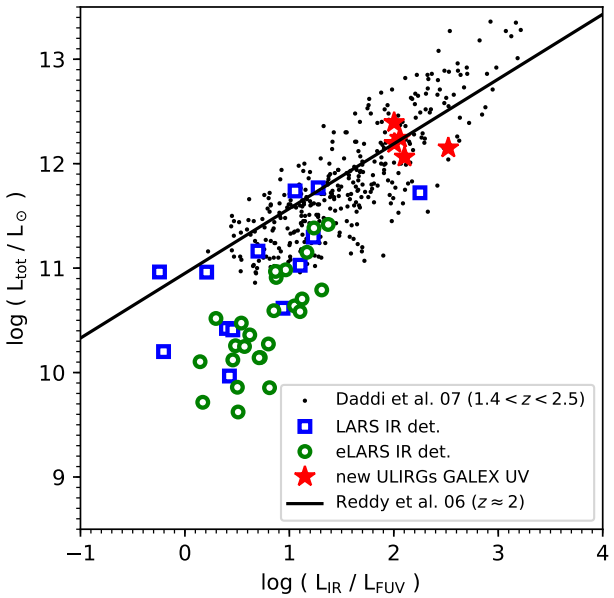

Figure 3.2: The figure shows a comparison of total bolometric luminosity vs ratio of infrared and FUV luminosity for galaxies. Black dots show the observed luminosities for infrared bright galaxies in redshift range $1.4 < z < 2.5$ (Daddi et al. 2007). Black line shows the best fit line for infrared excess with total bolometric luminosity (Equation 5 in Reddy et al. (2006)) obtained using IR bright galaxies at $z \approx 2$. Square represent the luminosities for LARS (blue) and eLARS (green) galaxies for which IR luminosities were available from WISE or IRAS catalog. Stars represent galaxies in current sample. Current sample does Lyα imaging in an unexplored IR bright luminosity range of galaxies.

[8] Wide-field Infrared Survey Explorer

Chapter 4

HST observations

Following survey strategy explained in Section **??**, we observed all five ULIRGs using four SBC long pass filters - F125LP, F140LP, F150LP, F165LP and two WFC filters F775W, FR782 installed on HST.

- The SBC detector is a single CsI micro-channel plate (MCP) with a multi-anode microchannel array (MAMA, hereafter) readout. It is a photon-counting device which processes events serially. SBC has a field of view of $34.6'' \times 30.8''$ with a pixel scale of $0.034'' \times 0.030''$. Raw images in SBC filter are 1024×1024 pixel.
- The WFC detector is a mosaic of two 2048×4096 Scientific Imaging Technologies (SITe) charge-coupled devices (CCDs). Field of view for WFC images is $202'' \times 202''$ with a pixel scale of $0.05''$per pixel and wavelength range from 3500-11000Å.

A total of 20 orbits spanning from Apr 1 2015 to Dec 30 2015 were proposed as a part of cycle 22 GO proposals of HST. HST data can be found on *Mikulski Archive for Space Telescopes* (MAST) [1] , under proposal ID 13655 (PI, Hayes M.). Exposure times of each exposure are listed in Table A.1. Exposure times were computed based on the requirement of reaching $S/N = 5$ with filter continuum of F165LP.

[1] https://archive.stsci.edu/hst/search.php

Chapter 5

Data Analysis

5.0.1 Creating Flat fielded images

Observations provide raw images in multiple exposures. Basic steps to convert the the raw images to flat fielded images is performed by `CALACS`[1] software. In short, pipeline does the following corrections to raw images:-

- Bias subtraction
- Correction for crosstalk between amplifiers during read out
- Remove bias stripping
- Correct for charge transfer losses during CCD readout[2]

Wide field Camera uses charged couple device (CCD) to read out the intensity of incident photons. Electrons are transferred on the CCD to readout the final signal. However, defects in silicon chip of CCD can lead to inefficient readout [3] . Inefficient readout not only reduces source flux, but it also adds a systematic shift in the object centroid as the trapped charge is slowly released during readout. The defects are mostly produced by radiation damage on the chip as telescope passes through South Atlantic Anomaly. `CALACS` corrects for this inefficiency while creating flat fielded images. The

[1] http://stsdas.stsci.edu/download/calacs/calacs.html
[2] Not applicable to SBC, as SBC is a MAMA detector not a CCD. More details in Section **??**.
[3] http://www.stsci.edu/hst/wfc3/ins_performance/CTE/cte.pdf

output of CALACS is a flat fielded image of galaxies in each exposure with association files identify different exposures.

5.0.2 Dark current subtraction for SBC

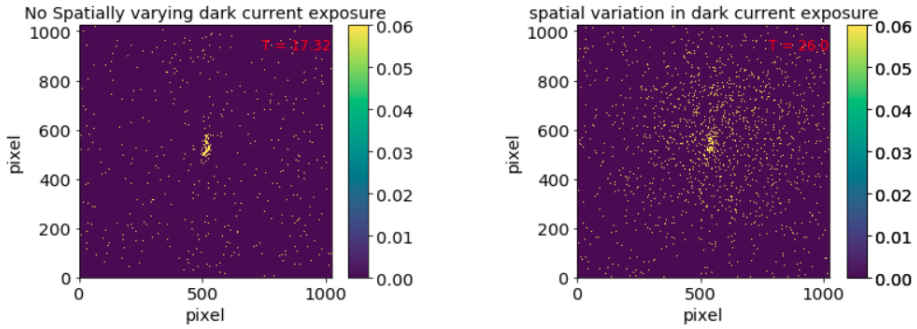

Figure 5.1: Two exposures of ULIRG 1 in same filter F165LP showing variation spatial variations in the counts outside main galaxy. Additional glow in right image is due to dark current which have spatial variations at higher temperature of SBC detector. Temperature of detector is shown at top right corner of the image. Fluxes are in arbitrary units scaled according to exposure times.

Counts in SBC detectors detectors are affected by temperature of the detector. Dark currents are the additional counts appearing on the image only due to the temperature of the detector. The Mikulski Archive for Space Telescopes (MAST) contains SBC dark images obtained from a variety of programs. Observations of dark current have shown that the dark counts take a constant value of 8.11×10^{-6} (counts /sec/pixel) [4] . It remains constant throughout the image as long as temperature of detector is below 25 degree Celsius. Once, the temperature of detector rises above 25°C, dark currents start to show a spatial variations on the image as shown in figure of Appendix A.1. Therefore, to remove the effects of dark current, one needs subtract the dark corresponding to the temperature of the detector. However, our analysis on dark currents has shown that the dark corresponding to the temperature of the detector does not minimize the thermal spatial variations (Details in Appendix A.1). We are still working on an improved dark subtraction method. For data analysis in present work, we are excluding all exposure which require the spatially varying dark current correction and subtracting a constant

[4] http://www.stsci.edu/hst/acs/documents/isrs/isr1704.pdf

value obtained by finding the mean of counts in the outer 200 pixels. This takes care of dark and sky subtraction simultaneously for all the exposure with temperature less that 25°C.

5.0.3 Aligning the FLT images

As described in Section **??**, Lyα imaging method is based on pixel to pixel flux density subtraction. This is why the astrometry of images in various filters needs to accurate and images in each exposure have to be aligned properly. If images are not aligned, one will observe artifacts of misalignment in the Lyα emission maps in place of real Lyα emission. Standard method of aligning galaxy images in two different filters uses bright stars as sources and aligns the images based on the positions of the stars. Owing to its large field of view, WFC images have many point sources in the full image which can be used to align and combine images in different exposures. However, one cannot use the same technique for SBC filter images because of lack of point sources (stars) in small field of view. Therefore, final images obtained from HST pipeline can not be used directly to obtain Lyα maps. Lack of point sources in SBC images make the astrometric correction a non-trivial task.

Assuming that large scale structure in nearby SBC UV filters is approximately same, the problem of aligning the images can be solved by using cross correlation between images. We maximize the cross-correlation between images to find the linear shift between different images of filters. To obtain the appropriate shift, 2D space of (δx, δy) is spanned with cross correlation matrix between images evaluated at each pixel of the image :-

$$\hat{I} = \frac{\sum_{i,j} I[i+\delta x, j+\delta y]}{nx * ny}$$

$$\hat{R} = \frac{\sum_{i,j} R[i,j]}{nx * ny}$$

$$X(\delta x, \delta y) = \frac{\sum_{i,j}(I[i+\delta x, j+\delta y] - \hat{I}) * (R[i,j] - \hat{R})}{\sqrt{\sum_{i,j}(I[i+\delta x, j+\delta y] - \hat{I})^2}\sqrt{\sum_{i,j}(R[i,j] - \hat{R})^2}}$$

Where I(x,y) and R(x,y) are fluxes at (x,y) positions of input and reference images respectively and $X(\delta x, \delta y)$ is cross-correlation between images. `xregister` task of IRAF

enables us to align images based on the correlation peaks in the images. However, it does not align the images which are rotated with respect to each other or images which are on different pixel scale. In our sample, HST images are obtained in different visits therefore the frames are rotated with respect to each other. In order to get properly aligned images in various SBC filters we first need to rotate the images to bring them to North up direction. In summary:-

- For each galaxy, images obtained on different visits of HST are identified based on observation dates. These images generally have different orientation. Therefore, images are rotated to find final image along North up direction.

- Next, use `xregister` to align the images with large enough window size to encompass the the shifts. Choosing proper reference image and choosing proper window size are two most important factors in getting proper alignment. It gives better alignment if brightest image is used as reference. Correlation peaks with bright image as reference can be easily resolved and shifts can be determined more accurately.[5]

This process gives us well aligned UV images in all SBC filters.

5.0.4 Stacking the FLT images

After aligning the FLT images, next step is to combine multiple FLT exposures to obtain final image in each filter. We are going to do a comparative study of SBC and WFC images. Therefore, images in both the filters have to be on same resolution scale. SBC has an average resolution scale of 0.033 $''$ per pixel while WFC has a resolution scale of 0.05 $''$per pixel. We combine images on a pixel scale of 0.05$''$per pixel so that we do not loose any information.

IRAF's `astrodrizzle`[6] task is used to combine the images in different exposures. It takes care of geometric distortions in the image. In short, it follows the following steps to combine the images :-

- Mask bad pixels from data

[5] Interpolation type in each process is chosen such that no artifacts of interpolation arise in the aligned images.

[6] Configuration file for astrodrizzle is provided in Appendix A.4

- Apply geometrical distortion maps
- Define world coordinate system (WCS[7] , hereafter) for images
- Remove Cosmic rays
- stack the images

After combining images for each filter on a pixel scale of 0.05, we align WFC images using `xregister` and then align the drizzled outputs of WFC images with the reference UV image chosen before. This way, we finally obtain images in each of WFC and SBC filter with correct astrometry.

5.0.5 PSF matching

Next step is matching the Point Spread Functions (PSFs) of drizzled images. PSF-matching is an important step in our analysis. We obtain images by pixel to pixel subtraction of images in two different filters. Therefore, if PSFs are not properly matched, final image may have structures appearing just because of unmatched PSFs. For SBC filters, in the central region the PSF is dominated by F165. The Figure 5.2 shows aperture photometry results on PSFs of 4 SBC filters. We choose broadest SBC filter PSF as reference and constructed kernel of transformations for other SBC filter PSFs. These kernels are then convolved with the images to obtain psfmatched image in each filter. We have used IRAFs `psfmatch` to match the PSFs. Consequently, Lyα maps produced in the present work may have diffused regions with unmatched PSFs. We are still working on PSF-matching for WFC images.

5.0.6 Sky subtraction

After obtaining the PSF matched images, 10 $\times$ 10 pixel boxes on all 4 sides of the images are selected. The median of pixel values from each box is chosen as the sky value. The sky subtracted images are then used for line map calculations.

[7] A conversion map to convert from pixel coordinates to RA and DEC position in the sky.

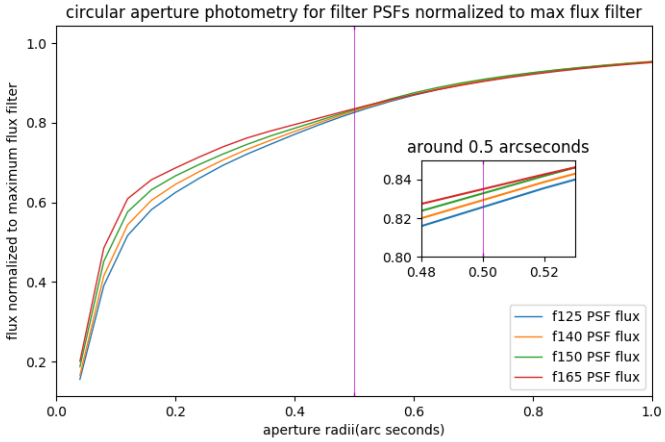

Figure 5.2: The figure shows circular aperture photometry of 4 SBC filters. Aperture photometry at 0.5 arc seconds gives F165 as largest width PSF. Therefore, for PSF matching PSF for F165 is used to obtain kernels for all other filters which are then PSF matched using convolution.

Chapter 6

Results

6.0.1 Line maps

Lyα continuum level and shape both are affected by dust content and stellar population very rapidly. In this section, we elaborate on the Lyα continuum subtraction method presented in Section **??**. Before we proceed, we multiply each image with `PHOTFLAM` keyword in the header to convert flux densities units from electrons/s to [`ergs/sec/arcsec`^{2}`/cm`^{2}]. Next, we define flux densities in filers F125, F140, F150, F165 as $f_{125}, f_{140}, f_{150}, f_{165}$ respectively. Flux densities in synthetic filers F125-F140, F140-F150, F150-F165 are defined as $f_{UV}^{blue}, f_{UV}^{line}, f_{UV}^{red}$.

$$f_{UV}^{blue} = f_{125} - f_{140}$$

$$f_{UV}^{line} = f_{140} - f_{150}$$

$$f_{UV}^{red} = f_{150} - f_{165}$$

Pivot wavelengths[1] for each of the synthetic filter are given by $\lambda_{blue}^{p} = 1309.26$Å, $\lambda_{red}^{p} = 1551.94$Å and $\lambda_{lya}^{p} = 1415.19$Å.

For each pixel (x,y) we obtain continuum emission at Lyα wavelength using linear

[1] Pivot wavelength of a filter $\lambda_p = \left[\frac{\int Q(\lambda)T(\lambda)d\lambda}{\int Q(\lambda)T(\lambda)d\lambda/\lambda}\right]^{1/2}$ where $T(\lambda)$ transmission of filter and $Q(\lambda)$ is overall response of the filter. $Q(\lambda) \times T(\lambda)$ is obtained using `pysynphot`.(http://pysynphot.readthedocs.io/en/latest/)

fitting for continuum on both sides of the line.

$$f_{lya}^{cont}(x,y) = \left(\frac{f_{UV}^{blue} - f_{UV}^{red}}{\lambda_{blue}^{p} - \lambda_{red}^{p}}\right)(\lambda_{lya}^{p} - \lambda_{blue}^{p}) + f_{UV}^{blue}(x,y) \tag{6.1}$$

Continuum subtracted line emission for Lyα is given by:-

$$F_{lya}(x,y) = [\{f_{140}(x,y) - f_{150}(x,y)\} - f_{lya}^{cont}(x,y)] \times \Delta\lambda^{FWHM} \tag{6.2}$$

Where $\Delta\lambda^{FWHM} = 105.10$Å represents the width of synthetic narrow band filter on Lyα line(i.e. the filter created using F140 and F150).

Starburst galaxies are often probed using Hα imaging. Continuum subtracted Hα images are obtained using a narrow band filter and a broad band filter installed on Wide Field Camera (WFC, hereafter) of HST. Ramp filter FR782 centered at $\lambda = 7599$Å is used for narrow band imaging. F775W broad band filter is used to image Hα continuum. The Figure 6.1 shows the throughput profiles in each filter. Broad band is used to subtract $H\alpha$ continuum while narrow band is used for $H\alpha$ line image. Matthee et al. 2015 suggest the following correction for line flux calculated after subtracting a broad band continuum image from narrow band image:-

$$f_{H\alpha} = \Delta\lambda_{NB} * \frac{f_{NB} - f_{BB}}{1 - \frac{\Delta\lambda_{NB}}{\Delta\lambda_{BB}}}$$

Where $f_{H\alpha}$ represents total $H\alpha$ line flux after continuum subtraction. $\Delta\lambda_{NB}, \Delta\lambda_{BB}$ represent width (FWHM) of narrow band and broad band respectively[2] . However, in the case of FR782 narrow band and F775W broad band filters $\Delta_{NB} << \Delta_{BB}$ the expression becomes-

$$\lim_{\Delta\lambda_{NB}\to 0} f_{H\alpha} = \Delta\lambda_{NB}(f_{NB} - f_{BB})$$

Therefore, we just use the filter width of narrow band filter to obtain line flux in Hα . Width of Hα narrow band filter is given by $\Delta\lambda^{FWHM} = 136.88$Å.

Following the steps in data reduction pipeline [3] , we obtain line and continuum images in Lyα and Hα wavelengths. These images can be used for photometric analysis. Figure 6.2 shows line maps for Lyα , Hα and FUV wavelengths. Out of 4 SBC bandpass filters, F165LP is the only filter which does not cover Lyα line (see Figure 2.1), therefore

[2] NB = Narrow Band, BB = Broad Band

[3] http://homepages.spa.umn.edu/~sourabh/projects/ULIRG/web/_build/html/index.html?

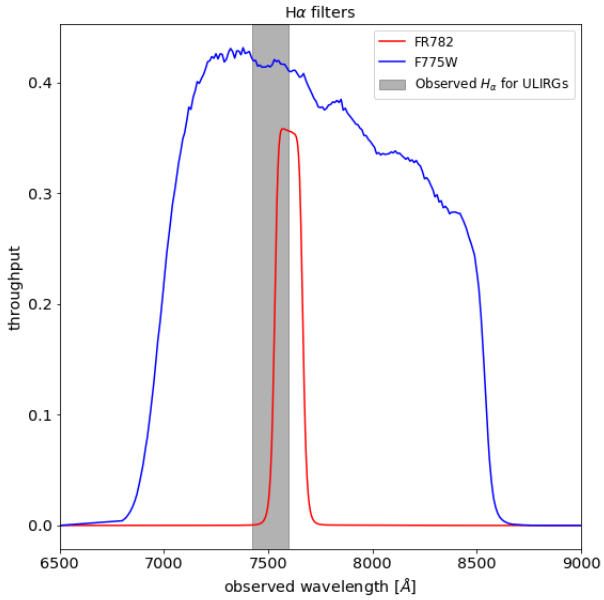

Figure 6.1: The figure shows narrow band and broad band throughputs for FR782 and F775W WFC filters respectively. The vertical Grey shaded area indicates the redshifted Hα wavelength range for galaxies in our sample.

we used the image in F165LP as a representative for FUV images. F125LP filter has the highest throughput amongst all SBC filter. The brightest pixel in F125LP image is chosen as the center of the image [4] . Drizzled outputs are the images with pixel scale of 0.05 $''$per pixel. We present results killoparsecs. In the Figure 6.2, we are showing inner 160, 240, 240, 300, 300 pixels of ULIRGs respectively which correspond to inner 22, 32, 32, 42, 34 kpc of the ULIRG. The number in colorbar on top of the figure represents $\texttt{fluxdensity}[\texttt{ergs/sec/arcsec}^2] \times 10^{20}$. A linear stretching is used to show images within the limits corresponding to colorbar (Refer Appendix A.5).

First column of the figure shows the continuum subtracted Lyα maps with overlaid red contours of Far Ultraviolet flux density. The second column shows only Lyα image where black represents emission while white represents absorption. The third column shows FUV images of galaxies. The fourth column shows continuum subtracted Hα images. The color map for each image is different (Details in Appendix A.5). We

[4] For ULIRG-3 brightest pixel was a pixel on the edge of the F125LP image which corresponds another bright UV region. This region was excluded for finding the center of the image.

discuss the details of these maps in Section **??**.

6.0.2 Local properties

6.0.2.1 Surface brightness profiles

In order to compare our results with the galaxies Lyman Alpha Reference Sample (LARS) (Hayes et al., 2014), we perform aperture photometry on Lyα , FUV and Hα images. Aperture photometry on galaxies gives information about the total emission and absorption from galaxies as we move away from the center of the galaxy. The Figure 6.3 shows surface brightness profiles for all 5 ULIRGs. First column shows the mean surface brightness in an annuli

$$S(r) = \frac{1}{\pi(r+\Delta r)^2 - r^2} \sum_{r<\sqrt{((x-x_0)^2+(y-y_0)^2)}<r+\Delta r} f^{kpc}(x,y)$$

Where r is radius of the circular aperture, $\Delta r = 2$ pixel is the width of circular annuli, $f^{kpc}(x,y)$ is line flux for Lyα and Hα (for UV it is flux density) at pixel position (x,y) and (x_0,y_0) are the center of the galaxy chosen using brightest F125 pixel (same as Figure 6.2). UV flux densities are very small to be presented on the same plot. We present UV flux density $\times 100$ on the plot. Distance from center is represented in logarithmic scale. We use physical scale in kiloparsec for "surface brightness". Surface brightness has units of $\mathtt{ergs-s^{-1}kpc^{-2}}$. e.g. For ULIRG-1 at z = 0.158, a pixel with an observed surface brightness of $\mathtt{10^{-18}ergs^{-1}cm^{-2}arcsec^{-2}}$ has an intrinsic rest-frame surface brightness of $\mathtt{9.16\times 10^{36}erg-s^{-1}kpc^{-2}}$ for our assumed cosmology. [5]

The second column of the figure shows cumulative luminosity for galaxies i.e.

$$L^t(r<r_0) = 4\pi d_L^2 \times \sum_{\sqrt{(x-x_0)^2+(y-y_0)^2}<r_0} f^{arcsec}(x,y)$$

where

[5]

$$SB_{kpc} = SB_{arcsec} * \frac{4\pi * d_L^2}{scale * scale}$$

where d_L is luminosity distance in cm and scale is the conversion of arcseconds to kpc at a given redshift. For ULIRG-1, $d_L = 754.9 Mpc$ and scale = 2.729 kpc/arcseconds

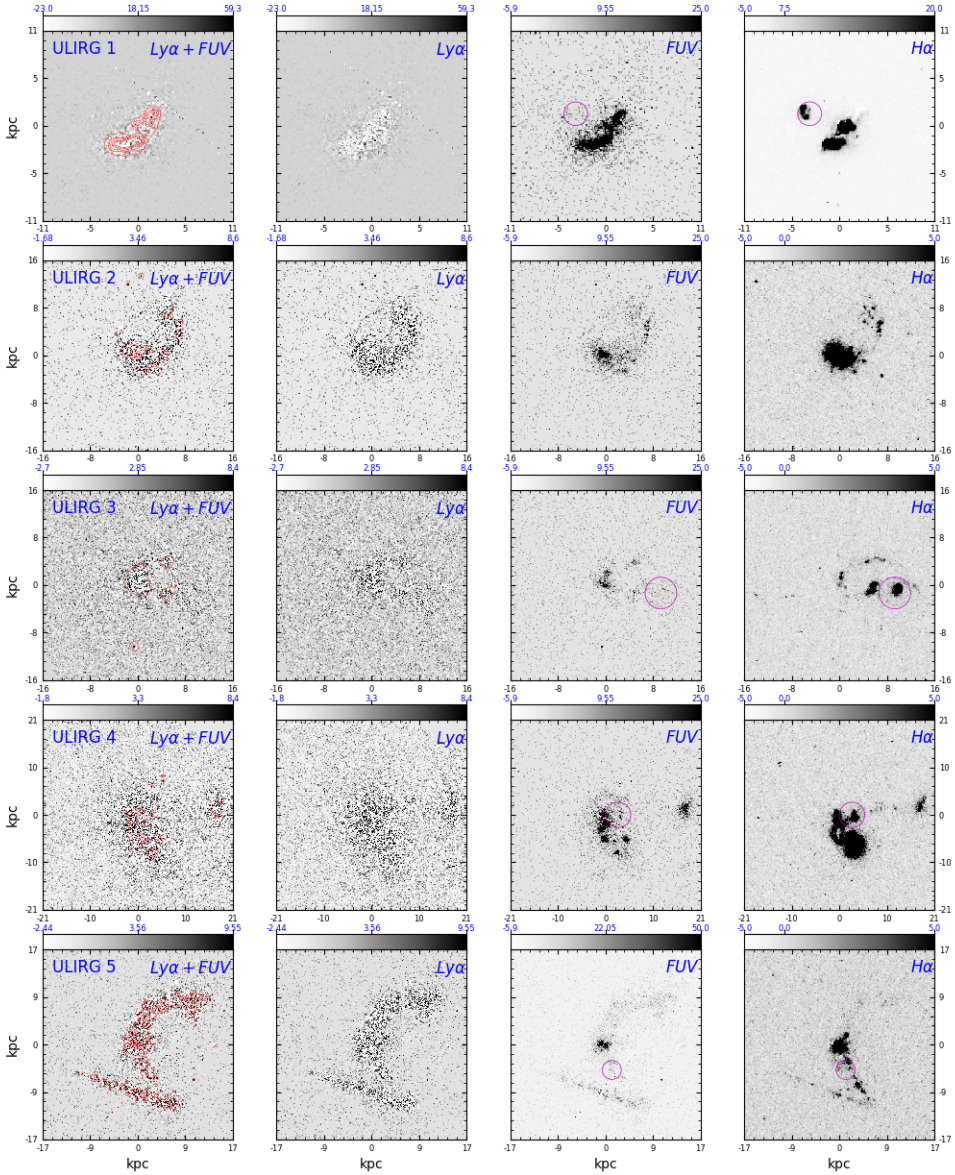

Figure 6.2: The figure shows final continuum subtracted line maps for Lyα , Hα for each ULIRG. F165LP image is used for FUV image. The first and second column show Lyα maps white representing absorption and black emission. Red contours on left most picture represent FUV contours of 5 intensities varying linearly between $I_{min}^{contour}$ $I_0 * 0.3$, where I_0 is the maximum FUV intensity and $I_{min}^{contour} = [0.05, 0.02, 0.01, 0.01, 0.02]$. White points represent absorption in Lyα maps while black points represent the emission. The color cuts for each images are different and scaling is linear between the color cuts (See Section **??** and A.5 for details).

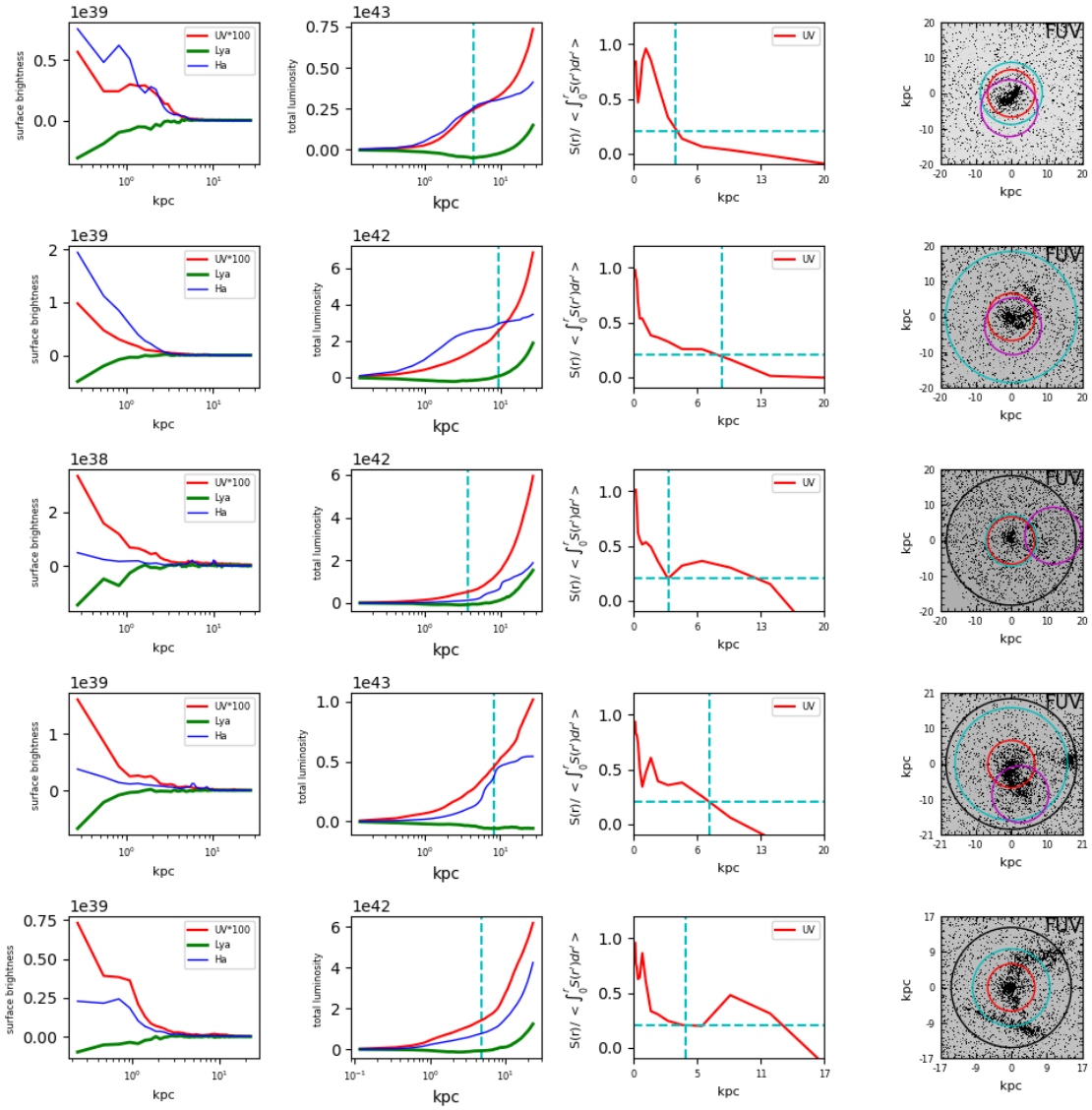

Figure 6.3: Surface brightness profiles for ULIRGs. Surface brightness is in the units of $ergs/sec/kpc^2$. The first column shows the surface brightness profile for $Ly\alpha$ (green), $H\alpha$ (blue) and UV (red). The second column shows the total luminosity in the aperture of a given radius in the units of ergs/s. The cyan line represents the $2 * r_{P20}$ which is calculated using the figure on the center left. The Cyan line represents the value of 0.2 which determines the petrosian radius for the galaxy. Right most panel shows UV image of galaxy obtained using SBC F165 flux (same as 6.2). The aperture in black color represents the largest radii annulus used to evaluate surface brightness, cyan circle represents the $2r_{P20}$, HST COS aperture is shown in red and SDSS aperture is shown in Magenta. It is clear that measuring the flux within petrosian radius does not always give the full flux from the galaxy. (see Section 6.0.3)

- For UV $f^{arcsec}(x, y)$ is flux density in units of $\mathtt{ergs} - \mathtt{s}^{-1}\mathtt{cm}^{-2}\mathtt{arcsec}^{-2}\mathring{\mathtt{A}}^{-1}$
- For Lyα and Hα , $f^{arcsec}(x, y)$ is line flux in units of $\mathtt{ergs} - \mathtt{s}^{-1}\mathtt{cm}^{-2}\mathtt{arcsec}^{-2}$
- d_L is luminosity distance of the galaxy in $\mathtt{cm}$.

6.0.2.2 Petrosian radius

The third column in the Figure 6.3 shows the plot for determining aperture size for to compare global properties of galaxies (Details in section 6.0.3). Petrosian 1976 introduced an aperture radius which is independent physical size of galaxy and depends only of surface brightness of galaxies. Petrosian radius (r_P)is defined as the radius at which ratio of average surface brightness at a given radii to average surface brightness inside that radius reaches $\eta = \eta_{cutoff}$ and $\eta(r)$ is defined by

$$\eta(r) = \frac{S(r)}{< S(< r) >}$$

where S(r) represents the average flux at the radius r. Hayes et al. 2014 use an aperture defined by (2 $\times$ petrosian radius) of the galaxy based on UV flux of galaxies. We also make same measurements on our galaxies for comparison. Figure 6.3 shows $\eta(r)$ and horizontal cyan lines indicate the value $\eta = 0.2$ which is used to determine Petrosian radius.

The fourth column of the Figure shows 6.3 the same FUV shown in third column of Figure 6.2. Various apertures are also marked on the figure. Cyan represents $2\times r_P$ aperture used to study global properties, black represents corrected aperture based on FUV size of galaxies (details in Section 6.0.3, table 6.1), SDSS fiber RA and Dec define center for SDSS aperture ($3''$) shown in magenta and HST COS aperture ($2.5\ ''$) is shown in red (Section 8).

6.0.2.3 Equivalent Widths

Equivalent width of a spectral line is a quantitative measure its strength. In high redshift Universe, Lyman alpha emitters are identified as the galaxies with rest frame

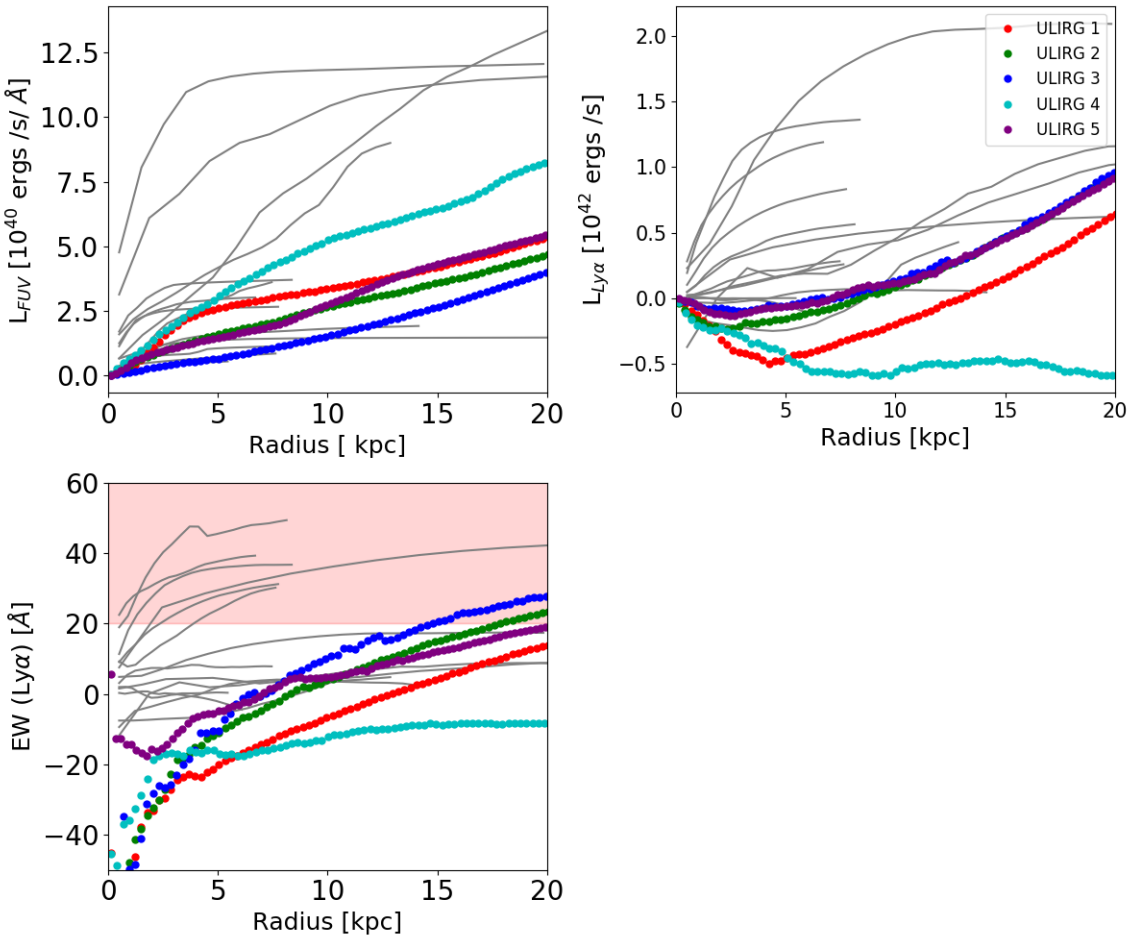

Figure 6.4: The figure shows a comparison of cumulative radial profiles of Lyα line flux, FUV flux density and equivalent width for LARS galaxies with ULIRGs in present sample. ULIRGs have similar FUV radial profiles as some of the LARS galaxies (shown in Grey). Bottom panel shows equivalent width of Lyα line. Red shaded area represents EW>20. ULIRG 2 and 3 have EW>20 at petrosian radius.

Lyα equivalent widths greater than 20. Rest frame equivalent width is given by :-

$$EW_\lambda = \frac{1}{(1+z)} \int \frac{1 - f_\lambda}{f_0} d\lambda$$

Where f_0 represents the continuum flux, f_λ represents flux at wavelength λ and z is the redshift of the galaxy. However, we do not have spectrum for ULIRGs to get f_λ. We use the ratio of Lyα line flux to FUV flux density to obtain the equivalent width and convert it to rest frame EW using the redshift of ULIRG. The Figure 6.4 shows cumulative profiles for Lyα line flux and FUV flux density along with a comparison to profiles from 14 LARS galaxies (Östlin et al., 2014). We identify that ULIRG 2 and 3 have EW >20 at petrosian radius. These galaxies could have similarities to high redshift LAEs. We explore this possibility in more detail in Section **??**.

6.0.3 Global properties

In this section, we study cumulative properties of line maps presented in **??** as a function of several galaxy properties. First step is to determine the size of the aperture for measuring total flux at a given wavelength. Observed size of galaxies decreases as we to higher redshifts. It makes comparison between photometry of galaxies non-trivial. Despite, the advantage of aperture petrosian radius estimate being size independent, the apertures based on petrosian radius do not work well for irregular galaxies. Owing to their large UV fluxes, star forming ULIRGs tend to be more irregular than normal elliptical or spiral galaxies (see Figure 6.3). Therefore, we selected an aperture based on UV size of galaxies to calculate total Lyα flux. Aperture radius are listed in Table 6.1. After calculating the total flux, it is converted to luminosity using $L_{Ly\alpha} = f_{Ly\alpha} * 4\pi d_L^2$. We find 3 out of 5 ULIRGs as Lyα emitters based on the aperture size as listed in 6.1. However, as it has been previously noted in Östlin et al. 2014, the selection of aperture size can convert a galaxy from Lyman alpha emitter to Lyman alpha absorber and vice-versa. In Figure 6.3, we also show an aperture that covers full UV image of galaxy so that there is loss of flux during aperture photometry. The flux values for these apertures are listed in Table 3.1. In the Section **??**, we discuss the aperture size problems in more details.

6.0.3.1 Infrared luminosity

Total infrared luminosity gives an estimate of dust in galaxies. We use infrared infrared luminosity obtained from IRAS surveys which is summing up fluxes in wavelength range of $8\mu m$ to $100\mu m$. (Martin et al., 2015) (CM15, hereafter) did a spectroscopic study of 11 ULIRGs in nearby Universe and found that 9 of 11 galaxies have Lyman alpha in emission. Based on their observation of broad optical emission lines and broad blue wings of Lyα emission spectrum, they predicted a power law relation between total Lyα luminosity and total far infrared luminosity ($L_{Ly\alpha} \propto L_{FIR}^2$). Relation is based on the physical picture of cool gas clouds condensing out of supernovae hot wind. Initial velocity of clouds gives broad nebular emission line wings while clouds are no disrupted because of acceleration by hot winds. The Figure 6.5 shows the relation between L_{FIR} and $L_{Ly\alpha}$ and a comparison with CM15 ULIRGs. Observations agree with CM15 ULIRGs. Dashed line in Figure 6.5, represent the porportionality constant for the relation between L_{FIR} and $L_{Ly\alpha}$ which depends on radius of starburst regions. To confirm consistencey with CM15, we next attempt to look for large velocity blue-shifted emission using the spectrum of these galaxies.

In Figure A.4 of appendix, we present the total Lyα luminosity as a function of total far infrared luminosity. We also show observations of IR fluxes for Lyman alpha reference sample LARS Östlin et al. (2014). Infrared luminosities for LARS galaxies were obtained from IRAS[6] and WISE[7] catalogs.

[6] http://irsa.ipac.caltech.edu/Missions/iras.html
[7] http://irsa.ipac.caltech.edu/Missions/wise.html

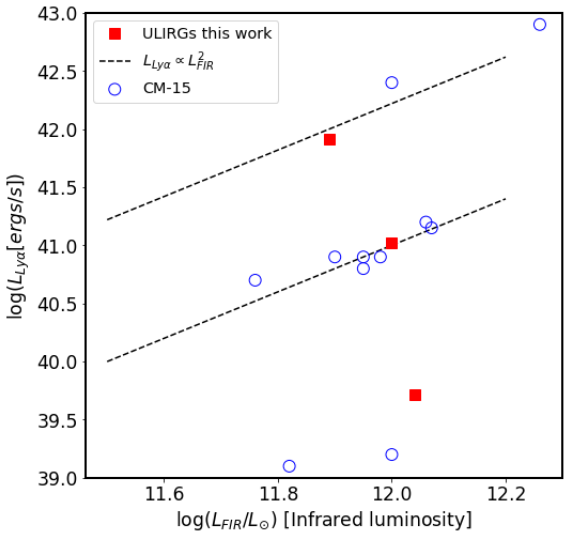

Figure 6.5: The figure shows the total Lyman alpha luminosity for 3 emitters as a function of far infrared luminosity. The total L_{FIR} is calculated by using $L_{FIR} = 3.86 \times 10^5 d^2_{MPc}[2.58F_\nu(60\mu m) + F_\nu(100\mu m)]L_\odot$(Murphy et al., 1996). The parallel lines show line with $L_{Ly\alpha} \propto L^2_{FIR}$ 6.3. A positive correlation between far infrared luminosity and Lyα luminosity is seen similar to Martin et al. 2015.

ULIRG ID	$2 \times r_{P20}$ (kpc)	L^{pt}_{UV} $(10^{42} cgs)$	$L^{pt}_{Ly\alpha}$ $(10^{41} cgs)$	$L^{pt}_{H\alpha}$ $(10^{42} cgs)$	L^{tot}_{UV} $(10^{42} cgs)$	$L^{tot}_{Ly\alpha}$ $(10^{41} cgs)$	$L^{tot}_{H\alpha}$ $(10^{42} cgs)$	Comments
1	8.95	3.19	-2.61	3.02	-	-	-	Lyα absorb
2	18.9	4.41	8.25	3.18	-	-	-	Lyα emitte
3	7.37	1.05	0.052	0.49	3.60	8.17	1.35	Lyα emitte
4	16.3	6.77	-4.76	5.24	7.95	-5.72	5.30	Lyα absorb
5	9.53	2.57	1.06	1.40	4.27	4.44	2.32	Lyα emitte

Table 6.1: This table lists the global measurements on line maps in Lyα , UV and Hα . First column has $2 * r_P$ petrosian radius. Columns, 2,3,4 represent total Lyman alpha luminosity in an aperture defined by petrosian radius. For ULIRG-3,4,5 , we identify an extended region to cover the full extent of galaxies represented as black circle in 6.3.

Chapter 7

Discussion

We have found above that 3 out of 5 ULIRGs in our sample have Lyα emission for a circular aperture of 2× Petrosian Radius. In terms of far infrared luminosity variations with Lyα luminosity, our results are consistent with the observations of Lyα emitters in local ULIRG sample of CM15 (Figure 6.5). In this section, we discuss our results based on plots and line maps.

7.0.1 Line maps

7.0.1.1 Comparison of UV and Hα

UV light follows young stellar population in galaxies. We identify bright UV knots near the center of each galaxy indicating the presence of young stellar population. There are a few regions that are bright in Hα but have very low flux in UV. These regions are shown with magenta circles in Figure 6.2. The features are most prominent in ULIRG-1,3,4,5. There are two plausible explanations of this observation:-

- It could be an indicator of recent star formation activity in the galaxy. UV luminosity from young stars takes more than 100 Myr to build up and contribute to UV emission. On the other hand, Hα is a recombination line which is easily observed in H-II regions.
- It could be just a dust obscured region along line of sight. Dust extinction from

galaxies generally decreases with increasing wavelength. It means that short wavelength photons are easily absorbed by dust than long wavelength photons. Therefore, dust attenuates UV photons more efficiently than Hα photons leading to regions with absent UV but booming Hα emission. This hypothesis is further reinforced by the fact that ULIRGs- 1,3,4,5 have larger infrared luminosities when comparison to infrared luminosity of ULIRG-2.

7.0.1.2 Sites for Lyα emission and absorption

First column of the figure Lyα maps with overlaid UV contours. We find that central regions of galaxies are dominated by Lyα absorption whereas scattered emissions are seen as we move away from central regions of galaxies. Emission in outer regions of galaxies can be explained by many scattering events of Lyα photons. This is why they are able to traverse a longer distance as they passes through ISM. Absorption from central regions could an indicative of vast reservoir of dust near the centers of galaxies.

7.0.1.3 A thin Stripe of bad pixels

MAMA detectors have a broken anode which disables rows 600 to 605 of images[1] . Owing to their large sizes, ULIRGs cover a large portion of SBC field of view. It is not possible to avoid the broken anode while taking the observations. This is the reason why we see straight lines passing through the images in Figure 6.2. For ULIRG-3 and 4, the stripe corresponding to broken anode passes near the center of the galaxy which causes unwanted distortions in images and lower S/N. The effects of unwanted pixels is less visible for ULIRG-1,2 and 5 because the stripe passes through pixels far from center which have less flux density.

7.0.2 Local properties results

The figure 6.3 shows the aperture photometry results for ULIRGs. First column of the figure shows surface brightness profiles. For ULIRG 2,3,4 UV flux is steeper than Hα , whereas for ULIRG 1,2 H$\alpha$is steeper than UV. This indicates that Hα and UV

[1] There are also a few dark spots at positions (334,977), (578,964), and (960,851) and bright spots at (55,281) and (645,102) with fluctuating rates. To avoid these regions on detector, the reference pixel for SBC has been moved to (512,400) Appendix A.1

morphologies of galaxies are different near the center. All Lyα profiles are dominated by absorption near the center of galaxy while Lyα emission adds up as we take larger apertures.

Second column in Figure 6.3 shows cumulative luminosity of ULIRGs. We expect the profile to flatten out at larger radii as the contribution from pixels at very large distance from galaxies should minimal. However, instead of observing a plateau for UV profiles, we find a rising trend in UV images and some of the Hα images as well. This could be the result of using a constant value for sky subtraction. This problem can be fixed either by modelling dark current more accurately (future work) or by subtracting the sky with a spatially varying 2D profile. For now, we move forward with a constant sky subtraction. Except for ULIRG 4, all Lyα profiles for every galaxy rises and becomes positive at large enough radius.

7.0.2.1 Global properties and apertures

In this section, we list out effects of aperture size on studies presented in this work. In addition to having a wide variety of morphologies, we do not have any constraints on inclination of starburst hosts of these galaxies. Hence no deprojection for ULIRGs can be applied. Circular apertures add a large number of background pixels because of irregular morphology of galaxies. This can give additional emission or absorption. However, if background subtraction is accurate, this effect can be minimized.

We have measured global properties using an aperture defined in 2$\times$ petrosian radius of galaxies. However, as shown in Figure 6.3, this aperture can be missing out flux from outer part of galaxies. Especially for ULIRG-3, majority of emisison comes from a region that is not included in the aperture defined by petrosian radius. For ULIRG-1, 2, petrosian radius works while fine but for ULIRG-3,4,5 we suggest using a larger aperure so that it covers full UV bright region (shown in black in 6.3).

In the fourth column of Figure 6.3 we have also shown apertures defined by SDSS fiber and aperture defined by COS. CM15 conclusions are based on COS results. However, as we can clearly see in the figure, COS aperure does not cover a large part of ULIRG flux. The results from CM15 are subjected to aperture losses from COS. Moreover, SDSS spectra obtained may also suffer from reduced flux because of aperture loss.

Therefore, one needs to be careful while comparing results of ULIRGs with results obtained from COS or SDSS apertures. In further studies, we are going to an aperture defined by segmentaion maps of galaxy to carry out isophotal photometry. We also attempt to look for angular variations in various isophotal mesaurements.

Chapter 8

Future works and follow up

This is an ongoing project. In brief, I am working on the following problems currently [1] :-

- Error maps for line map
- PSFmatching for WFC, new psf method in SBC
- proper model for dark currents in SBC
- Isophotal photometry
- SED modelling and merger history connection (based on Murata et al. 2017)
- PAH fraction using Spitzer spectrum in (2.5-5 μm)
- SFR , fesc determination using proper models, fesc, SFR
- Identifying signatures of using spectrum of ULIRGs outflows
- Lyα radiative transfer modelling in dusty mediums
- Identifying connected Lyα features using dendrograms [2]

[1] Some of the results may show up in presentation
[2] https://dendrograms.readthedocs.io/en/stable/

8.1 Follow up

Based on our experience with HST SBC and WFC filter images in this study, we find a few suggestions for future imaging studies with these filters :-

- One to one correspondence between dark current image and temperature of the detector does not always work for SBC filter. A more accurate modelling of spatial variation of dark current is required.

- The world coordinate system (WCS) on reduced HST SBC images are not accurate as we found a misalignment amongst in images up to 30 pixels. The issue arises because of missing point sources (stars) to align the images. For future surveys, we suggest taking a WFC filter image along with SBC image on the same visit. As WFC field of view is larger, one can align images using point sources and then use the WCS from WFC image as reference to set up WCS for SBC images.

With the accepted early science release proposal on LIRGs and ULIRGs in JWST (James Webb Space Telescope -launching in 2018*)(Armus et al., 2017), a well resolved imaging and spectroscopic study of LIRGs and ULIRGs will be obtained. The project will use NIRCAM and MIRI images to study the ISM on scales of 50-100pc in the nuclei of local Luminous Infrared Galaxies in local Universe. NIRSPEC and MIRI IFUs will also be used to take spectrum in wavelength range of 0.96-29 μm.

After finalizing our results on isophotal photometry, we attempt to follow up these ULIRGs using slit spectrograph on Magellan infrared spectrograph (MMIRS). It has multiple slits in wavelength range 0.9 -2.4 μm. Refractive optics on MMIRS offers a $6.9'' \times 6.9''$ field of view with a spatial resolution of 0.2 arcseconds per pixel. For ULIRGs in current sample we should be able to observe inner 18 kpc of the galaxy. We also attempt to obtain better optical spectrum for ULIRG in southern hemisphere using Cerro Tololo Inter-American Observatory (CTIO) or NOT (Nordic Optical Telescope).

Chapter 9

Summary

In summary, preliminary results from Lyα imaging of ULIRGs show that 3 out of 5 ULIRGs have Lyα in emission globally. Most of Lyα emission comes from outer regions of galaxies whereas central regions are dominated by Lyα absorption. Results are sensitive to the aperture size selection. Isophotal photometry is required to confirm that Lyα is not a result of summing over background pixels. Results are consistent with a physical picture cool gas clouds condensing out of supernovae hot wind. However, optical spectrum needs to be inspected to conclude this physical picture.

References

Armus, L., Appleton, P., Barcos-Munoz, L., et al. 2017, A JWST Study of the Starburst-AGN Connection in Merging LIRGs, JWST Proposal ID 1328. Cycle 0 Early Release Science

Baldwin, J. A., Phillips, M. M., & Terlevich, R. 1981, PASP, 93, 5

Berta, S., Magnelli, B., Nordon, R., et al. 2011, A&A, 532, A49

Bridge, C., Blain, A., Borys, C., Petty, S., & Farrah, D. 2012, WISE Discovered Ly-alpha Blobs at High-z: AGN Feeback Caught in the Act?, Spitzer Proposal

Chapman, S., Blain, A., Ivison, R., & Smail, I. 2005, Mid-IR spectroscopy of suspected very hot dusty, high-z galaxies, Spitzer Proposal

Chary, R.-R., Teplitz, H. I., Dickinson, M. E., et al. 2007, ApJ, 665, 257

Daddi, E., Dickinson, M., Morrison, G., et al. 2007, ApJ, 670, 156

Desai, V., Armus, L., Spoon, H. W. W., et al. 2007, ApJ, 669, 810

Díaz-Santos, T., Charmandaris, V., Armus, L., et al. 2010, ApJ, 723, 993

Dijkstra, M. 2014, , 31, e040

Galliano, F., Galametz, M., & Jones, A. P. 2017, ArXiv e-prints, arXiv:1711.07434

Hayes, M., Östlin, G., Mas-Hesse, J. M., & Kunth, D. 2009, AJ, 138, 911

Hayes, M., Östlin, G., Mas-Hesse, J. M., et al. 2005, A&A, 438, 71

Hayes, M., Östlin, G., Duval, F., et al. 2014, The Astrophysical Journal, 782, 6

Henry, A., Scarlata, C., Martin, C. L., & Erb, D. 2015, The Astrophysical Journal, 809, 19

Hummer, D. G., & Storey, P. J. 1987, MNRAS, 224, 801

Kauffmann, G., Heckman, T. M., White, S. D. M., et al. 2003, MNRAS, 341, 33

Kewley, L. J., Groves, B., Kauffmann, G., & Heckman, T. 2006, MNRAS, 372, 961

Kewley, L. J., Heisler, C. A., Dopita, M. A., & Lumsden, S. 2001, ApJS, 132, 37

Kim, D.-C., Veilleux, S., & Sanders, D. B. 1998, The Astrophysical Journal, 508, 627

Madau, P., & Dickinson, M. 2014, 1

Magnelli, B., Elbaz, D., Chary, R. R., et al. 2011, A&A, 528, A35

Martin, C. L., Dijkstra, M., Henry, A., et al. 2015, arXiv:arXiv:1501.05946v1

Matthee, J., Sobral, D., Santos, S., et al. 2015, MNRAS, 451, 400

Menéndez-Delmestre, K., Blain, A. W., Smail, I., et al. 2009, ApJ, 699, 667

Murata, K. L., Yamada, R., Oyabu, S., et al. 2017, MNRAS, 472, 39

Murphy, E. J., Chary, R.-R., Dickinson, M., et al. 2011, ApJ, 732, 126

Murphy, Jr., T. W., Armus, L., Matthews, K., et al. 1996, AJ, 111, 1025

Natta, A., & Panagia, N. 1984, ApJ, 287, 228

Östlin, G., Hayes, M., Kunth, D., et al. 2009, AJ, 138, 923

Östlin, G., Hayes, M., Duval, F., et al. 2014, The Astrophysical Journal, 797, 11

Pengelly, R. M. 1964, MNRAS, 127, 145

Petrosian, V. 1976, ApJ, 209, L1

Pope, A., Chary, R.-R., Alexander, D. M., et al. 2008, ApJ, 675, 1171

Reddy, N. A., Steidel, C. C., Fadda, D., et al. 2006, ApJ, 644, 792

Scarlata, C., Colbert, J., Teplitz, H. I., et al. 2009, ApJ, 704, L98

Shapley, A. E., Steidel, C. C., Pettini, M., & Adelberger, K. L. 2003, ApJ, 588, 65

Stacey, G. J., Hailey-Dunsheath, S., Ferkinhoff, C., et al. 2010, ApJ, 724, 957

Stark, D. P., Ellis, R. S., Chiu, K., Ouchi, M., & Bunker, A. 2010, MNRAS, 408, 1628

Veilleux, S., Kim, D.-C., & Sanders, D. B. 2002, ApJS, 143, 315

Verhamme, A., Schaerer, D., & Maselli, A. 2006, Astronomy and Astrophysics, 460, 397

Appendix A

Dark subtraction

A.1 Dark currents in SBC

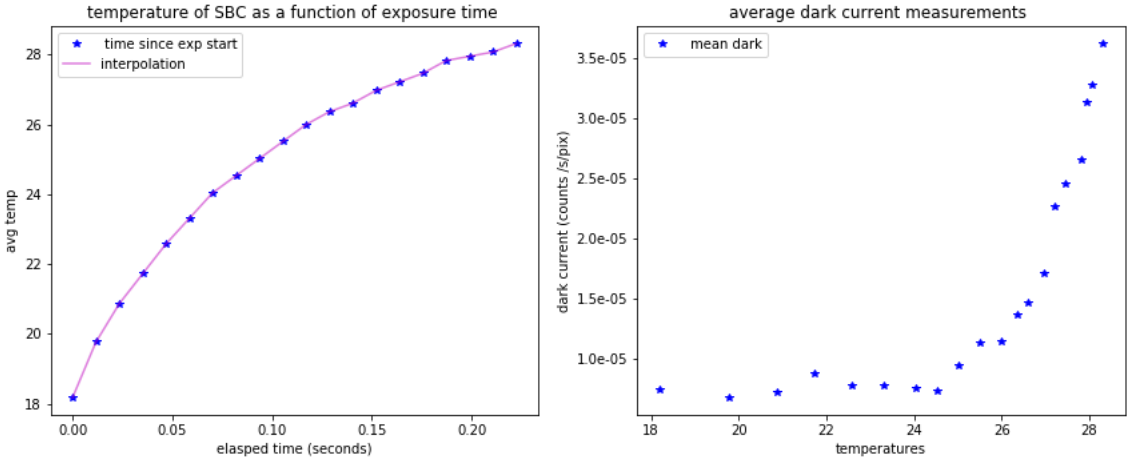

Figure A.1: Dark current measurements of SBC filters. Th detector temperature rises if the detector remains switched on for longer. It adds additional thermal noise in the data

A.2 Observation log

ULIRG id		UV filters				Optical filters	
	exposure info	F125	F140	F150	F165	F775W	FR782
1	$< T_{exp} >$	437	530	730	1020	1084	1090
	n_{exp}	3	3	3	3(2)	2	2
2	$< T_{exp} >$	437	530	720	1020	1084	1090
	n_{exp}	3	3	3	3(2)	2	2
3*	$< T_{exp} >$	380	477	657	870	1084	1090
	n_{exp}	6(3)	6(2)	6(4)	6(2)	2	2
4	$< T_{exp} >$	440	520	720	1000	1084	1090
	n_{exp}	3	3	5(3)	3(2)	2	2
5	$< T_{exp} >$	440	520	720	1000	1084	1090
	$< n_{exp} >$	3	3	3	3(2)	2	2

Table A.1: The table lists some details of HST observations of ULIRGs. Observations were taken in 2 HST visits. Some of the observations of ULIRG-3 and 4 were corrupted while a bunch of exposures had detector temperature $T > 25^oC$. The numbers in parenthesis indicate the exposures used to produce combined image in each filter.

A.3 CTE correction example

A.4 Configuration for astrodrizzle

Example of configuration file for `astrodrizzle`:-

```
adriz( 'jcmc21qtq_F125LP_allext_driz1_flt.fits,jcmc21rdq_F125LP_allext_driz1_flt.fits,
 jcmc22f0q_F125LP_allext_driz1_flt.fits',output='gal2_UV_F125',build=True, static=True,
  skysub=True,driz_separate=True,median=True,blot=True,driz_cr=True,driz_combine=True,
  final_wcs=True, final_rot=0.0, final_scale=0.05)
```

A.5 Color cuts for Line maps

Color cuts

```
<<<<<<<<<UV>>>>>>>>>>>>
vmin_UV = -5e-20
```

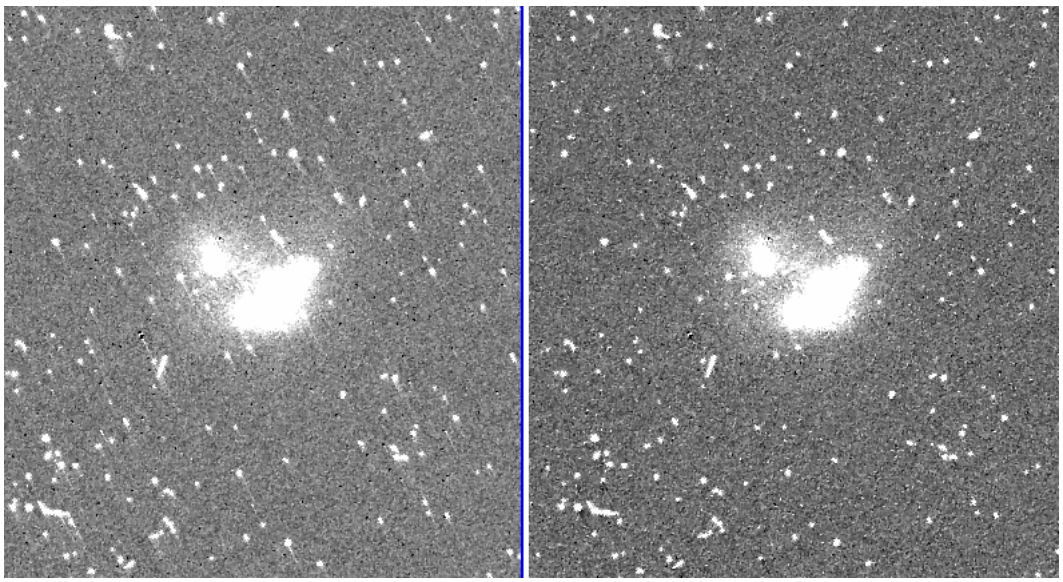

Figure A.2: The figure shows the CTE correction of images using CALACS algorithm for Hα image of ULIRG 1. The left figure shows the elongated pixels because of the presence of charge transfer loss during CCD read out. CTE corrected image is shown in right panel. The algorithm is described in http://www.stsci.edu/hst/acs/software/CTE/.

```
vmax_UV = np.array([5e-19, 5e-19, 5e-19, 5e-19, 1e-18] )/2.


<<<<<<<<<<<LYa>>>>>>>>>>>>
vmin_lya = ([-2.3e-19,-1.68e-20,-2.7e-20,-1.8e-20,-2.44e-20 ])
vmax_lya = ([5.93e-19, 8.6e-20, 8.4e-20, 8.4e-20, 9.55e-20] )

<<<<<<<<<<<<<HA>>>>>>>>>>>>>
vmin_ha = -5e-20
vmax_ha = ([2e-19, 5e-20, 5e-20, 5e-20, 5e-20] )
```

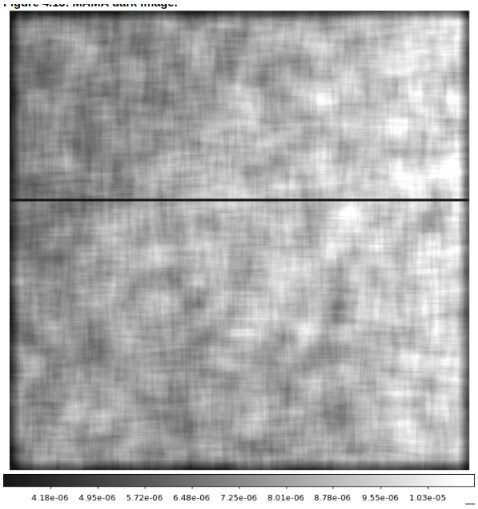

Figure A.3: MAMA dark image. The dark line near the center of the image is the effect of broken anode on SBC MAMA.

A.6 Flow chart

Flow chart of the algorithm steps

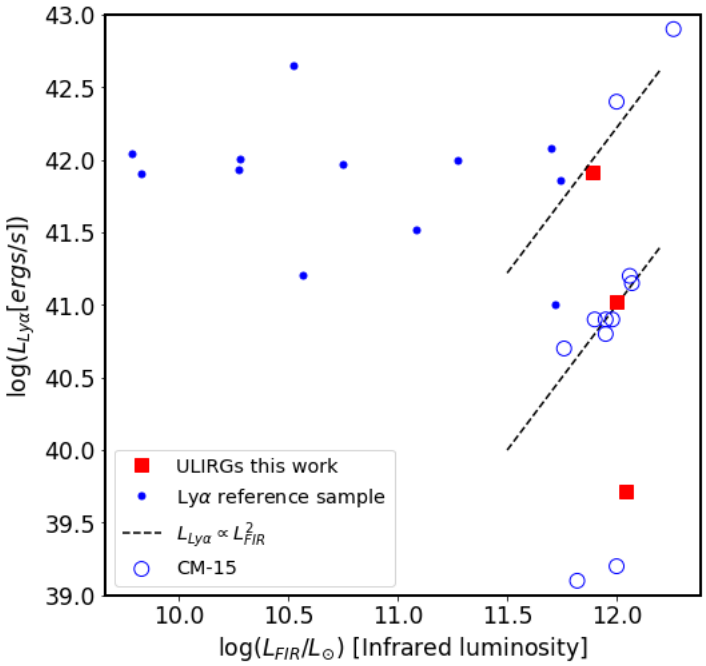

Figure A.4: The figure shows a plot infrared luminosity vs Lyα luminosity of LARS galaxies, CM15 galaxies and ULIRGs. Methodology to determine global luminosity is similar to LARS galaxies but our one can clearly see that LARS galaxies do not cover the regime of ULIRGs in sample and they do not follow rising trend similar to CM15.

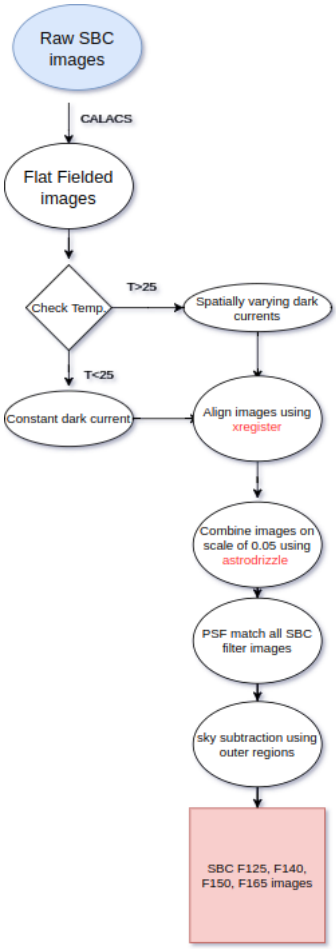

Figure A.5: The figure shows a plot lya reduction pipeline steps